LITHIUM DEPLETION OF NEARBY YOUNG STELLAR ASSOCIATIONS

ERIN MENTUCH, ALEXIS BRANDEKER[1], MARTEN H. VAN KERKWIJK, RAY JAYAWARDHANA
Department of Astronomy & Astrophysics, University of Toronto, 50 St. George Street, Toronto, Ontario M5S 3H4, Canada

AND

PETER H. HAUSCHILDT
Hamburger Sternwarte, Gojenbergsweg 112, 21029, Hamburg, Germany
Draft version August 27, 2008

ABSTRACT

We estimate cluster ages from lithium depletion in five pre-main-sequence groups found within $100\,\mathrm{pc}$ of the Sun: TW Hydrae Association, η Chamaeleontis Cluster, β Pictoris Moving Group, Tucanae-Horologium Association and AB Doradus Moving Group. We determine surface gravities, effective temperatures and lithium abundances for over 900 spectra through least squares fitting to model-atmosphere spectra. For each group, we compare the dependence of lithium abundance on temperature with isochrones from pre-main-sequence evolutionary tracks to obtain model dependent ages. We find that the η Chamaelontis Cluster and the TW Hydrae Association are the youngest, with ages of $12\pm6\,\mathrm{Myr}$ and $12\pm8\,\mathrm{Myr}$, respectively, followed by the β Pictoris Moving Group at $21\pm9\,\mathrm{Myr}$, the Tucanae-Horologium Association at $27\pm11\,\mathrm{Myr}$, and the AB Doradus Moving Group at an age of at least $45\,\mathrm{Myr}$ (where we can only set a lower limit since the models – unlike real stars – do not show much lithium depletion beyond this age). Here, the ordering is robust, but the precise ages depend on our choice of both atmospheric and evolutionary models. As a result, while our ages are consistent with estimates based on Hertzsprung-Russell isochrone fitting and dynamical expansion, they are not yet more precise. Our observations do show that with improved models, much stronger constraints should be feasible: the intrinsic uncertainties, as measured from the scatter between measurements from different spectra of the same star, are very low: around $10\,\mathrm{K}$ in effective temperature, $0.05\,\mathrm{dex}$ in surface gravity, and $0.03\,\mathrm{dex}$ in lithium abundance.

Subject headings: open clusters and associations: individual (η Chamaelontis, TW Hydrae, β Pictoris, Tucanae-Horologium, AB Doradus) — stars: abundances — line: profiles — stars: pre-main-sequence

1. INTRODUCTION

Triggered largely by the discovery of young stars in the *ROSAT* X-ray Satellite All-Sky Survey, over the last decade several nearby pre-main-sequence (PMS) star groups have been identified (for a review, see Zuckerman & Song 2004). Ranging in age from roughly $6\,\mathrm{Myr}$ to $\sim100\,\mathrm{Myr}$, five separate groups can be distinguished: TW Hydrae Association (TWA), η Chamaeleontis cluster (η Cha), β Pictoris Moving Group (BPMG), Tucanae-Horologium association (TUCHOR) and AB Doradus Moving Group (ABD). The common space motions and localized sky positions suggest that these groups are likely connected to the Sco-Cen star forming region located $\sim100\,\mathrm{pc}$ away in the southern hemisphere. Mamajek et al. (1999) and Song et al. (2003) have traced back the space motion of members in BPMG, TWA and η Cha and argue that the groups are related to a star formation burst in the Sco-Cen region as a result of the passing of the Carina arm $\sim60\,\mathrm{Myr}$ ago.

These groups, because of their close vicinity, are excellent laboratories for studying star and planet formation. Well constrained ages are necessary to make conclusions about timescales of, e.g., disk dissipation and planet formation. Already, observations from the same sample presented in this paper have revealed that accretion disks can last up to $\sim10\,\mathrm{Myr}$, but beyond this is rare (Jayawardhana et al. 2006).

Previously, ages have been derived from Hertzsprung-Russell (HR) diagram fitting, group dynamics and lithium

abundance measurements. Luhman & Steeghs (2004) provide an HR diagram isochrone age for η Cha of $6^{+2}_{-1}\,\mathrm{Myr}$ derived from the evolutionary models of Baraffe et al. (1998; hereafter BCAH98) and Palla & Stahler (1999), which agrees well with the dynamical expansion age of $6.7\,\mathrm{Myr}$ determined by Jilinski et al. (2005). The dynamical age of TWA has been harder to determine because of inconsistent space motions among its more than 30 members. An inferred age of $8.3\pm0.8\,\mathrm{Myr}$ is given to TWA based on the dynamical motion of four members (de la Reza et al. 2006). However, the likely complex dynamical evolution of TWA has led to several plausible evolutionary scenarios. Makarov et al. (2005) attribute this complex evolution to a chance encounter with Vega, while Lawson & Crause (2005) suggest TWA is composed of two separate groups, based on bimodal rotation period distributions with distinctly separate ages of $\sim10\,\mathrm{Myr}$ and $\sim17\,\mathrm{Myr}$. More recently, Barrado y Navascués (2006) finds a conservative age of $10^{+10}_{-7}\,\mathrm{Myr}$ by comparing ages from HR diagram isochrone comparisons (from BCAH98) and lithium abundances.

The slightly older group BPMG has an estimated age of $12^{+8}_{-4}\,\mathrm{Myr}$ based on HR diagram isochrone comparisons (from BCAH98) and lithium abundances (Zuckerman et al. 2001), with three dimensional motions that are consistent with a dynamical expansion age of $11.5\,\mathrm{Myr}$ (Ortega et al. 2002). Feigelson et al. (2006) independently derived an age of $13^{+4}_{-3}\,\mathrm{Myr}$ for the recently confirmed wide binary system of 51 Eri and GJ 3305, part of BPMG.

Known to be older than BPMG, but younger than the Pleiades, TUCHOR has an age of 20–$40\,\mathrm{Myr}$ based on Hα

---

[1] Current address: Stockholm Observatory, AlbaNova University centre, SE-106 91 Stockholm, Sweden

measurements, X-ray luminosity, rotation and lithium abundances in comparison to other young clusters like TWA and the Pleiades (Zuckerman & Webb 2000; Stelzer & Neuhäuser 2000).

Perhaps, the most debated age is that of the ABD group. Zuckerman et al. (2004) derived an age of 50 Myr by comparing the Hα emission strength of ABD members to members of the younger TUCHOR association, in addition to fitting its three M-type members to HR diagram isochrones. In contrast, Luhman et al. (2005) compared HR isochrones of ABD members to those of two well-observed clusters with ages of 50 and 125 Myr and suggested that the ABD group is coeval with the Pleiades at an age of 100–125 Myr. The latter age is strongly supported by Ortega et al. (2007), who compute full 3D galactic orbits of ABD and the Pleiades cluster and show the dynamics of the two groups can be traced back to a common origin of 119 ± 20 Myr ago.

A relatively new approach to age estimates is to use the evolution of the lithium abundance for low-mass, partially and fully convective PMS stars (Bildsten et al. 1997; Jeffries & Oliveira 2005). The initiation and duration of lithium depletion in PMS stars is dependent on mass and is very sensitive to the central temperature. Lithium is converted into helium in p, α reactions in cores of low-mass stars when the temperature reaches 2.5×10^6 K. The lower the stellar mass, the longer the time it takes to reach this critical temperature. For example, a $0.6\,M_\odot$ star begins to burn lithium at an age of 3 Myr, while a lower mass star at $0.1\,M_\odot$ begins to burn lithium at an age of 40 Myr. Stars with $M < 0.06\,M_\odot$ never reach this typical temperature, while stars with $0.6\,M_\odot < M < 1.2\,M_\odot$ burn lithium for a short period (1–2 Myr) until a radiative core develops, and more massive pre-main sequence stars do not destroy lithium in their envelope at all. The result of these processes is a dip in the lithium abundance as a function of luminosity (and consequently, a function of effective temperature), only affecting stars with spectral types later than F5. As a group ages, this dip becomes deeper and widens on the cool end as progressively cooler stars reach the critical core temperature.

The cool end of this dip has been used to date coeval groups containing late M-dwarf stars by identifying the lithium depletion boundary (LDB). The LDB marks the luminosity above which all stars will have depleted their lithium. The lithium is very quickly depleted in these low-mass stars, so the LDB marks a sharp jump from initial to near depleted lithium abundances. As the temperature in the cores of PMS stars increases in time, the LDB will shift to cooler temperatures as a cluster ages. LDB ages have been determined for the Pleiades (125 ± 8 Myr), α Per (90 ± 10 Myr), IC 2391 (53 ± 5 Myr), and NGC 2547 (35 ± 4 Myr) (Stauffer et al. 1998; Barrado y Navascués et al. 1999; Stauffer et al. 1999; Barrado y Navascués et al. 2004; Jeffries & Oliveira 2005).

In this paper, we fit more than 900 multi-epoch, high-resolution spectra, introduced in §2, of 121 low-mass PMS stars to synthetic spectra created from PHOENIX model atmospheres (see §3). We begin by identifying the model with the best-fitting surface gravity, $\log g$, and effective temperature, $T_{\rm eff}$ for each observed spectrum, as described in §4. In §5, we use these best-fit $T_{\rm eff}$ and $\log g$ to find the lithium abundance by fitting model spectra to both the 6 104 Å and 6 708 Å lithium features in the observations, but now using lithium abundance as a free parameter. For comparison, we also measure the equivalent width (EW) of the 6 708 Å lithium doublet

which allows us to chronologically order the groups based solely on empirical measurements. We proceed by comparing the measured lithium abundance distribution to that predicted by PMS evolutionary models of BCAH98 and Siess et al. (2000) and estimate model dependent ages for each of the PMS groups.

2. OBSERVATIONS

High-resolution spectra were obtained during six separate observation runs, on a total of 19 nights, between December 2004 and April 2006, utilizing the MIKE spectrograph at the Magellan-Clay 6.5 m telescope on Las Campanas, Chile. MIKE is a double echelle instrument, covering two separate wavelength regions. For this study, the red region from 4 900 Å to 9 300 Å is used. The raw data were bias subtracted and flat-fielded, and before extraction, the scattered background in the spectrograph was subtracted by fitting splines to interorder pixels. The spatial direction of the projected slit produced by MIKE is wavelength dependent and not aligned with the CCD. We therefore extracted spectra using a custom procedure develped in ESO-MIDAS, that takes into account the tilt and optimally extracts the spectrum by iteratively estimating the slit illumination function. For wavelength calibration, exposures of a Thorium-Argon lamp were used, as well as observed telluric absorption lines. A more detailed account of the reductions and a log of the observations will appear in a forthcoming paper (A. Brandeker et al. 2008, in prep.). Multiple spectra for many of the targets in our sample were taken in order to search for multiplicity and perform variability studies.

With no binning and using the $0.''35$ slit, the spectra in this study have a resolution of R$\sim$60 000. The pixel scale was $0.''13$ pix^{-1} in the spatial direction, and about 24 m Å pix^{-1} at 6 500 Å in the spectral direction. Integration times were chosen so that the signal-to-noise ratio (S/N) $\gtrsim$70 per spectral resolution element at 6 500 Å, except for the brightest stars where this would have implied an exposure shorter than 120 s. In those cases, we used the longest exposure time shorter than 120 s that did not saturate the detector, giving (S/N) = 70–500, depending on seeing.

For this study, we only use objects with spectral types later than F5, and earlier than M5. Hotter stars do not show depleted lithium abundances in their atmospheres, because their cores are already radiative when lithium burning starts. Cooler stars were not included in the survey because they were too faint. We also exclude obvious spectroscopic binaries. In total we have a sample of 121 stars, with 11 from η Cha, 32 from TWA, 23 objects from BPMG, 35 from TUCHOR, and 22 from ABD. For comparison, we also analysed 20 radial-velocity standard stars from the field.

3. MODELS

We compute synthetic spectra using version 14 of the PHOENIX model atmosphere package (Hauschildt & Baron 1999). The model atmospheres are described in Kučinskas et al. (2005, 2006). In total, we have 240 model spectra covering a spectral region from 3 200 Å to 10 000 Å with 0.03 Å spectral resolution, with temperatures ($T_{\rm eff}$) ranging from 2 500 K to 6 500 K in steps of 100 K, and surface gravities ($\log g$) ranging from 3.0 to 6.0 in steps of 0.5 (i.e. gravities ranging from 10^3 cm s^{-2} to 10^6 cm s^{-2}). For each of these temperature and gravity combinations, we have additional models with different lithium abundances

(N_{Li}) ranging from $\log N_{\text{Li}} = 0.0$ to 4.0 in steps of 0.5 (where the normalization is such that $\log N_{\text{H}} = 12$), which cover the $6\,104\,\text{Å}$ and $6\,708\,\text{Å}$ lithium absorption lines. All models were calculated at solar metallicity.

The atmospheric models are calculated under the assumptions of local thermodynamic equilibrium (LTE). Carlsson et al. (1994) have systematically analyzed the effects of non-LTE on the formation of the Li I line in cool stars. They show that that the non-LTE effects can lead to discrepancies in lithium abundances measured from the $6\,708\,\text{Å}$ lithium doublet from about -0.3 to 0.3 dex depending on the depletion and temperature. We attempt to minimize the exclusion of non-LTE effects by also fitting the $6\,104\,\text{Å}$ lithium feature whose non-LTE corrections are opposite to those of the $6\,708\,\text{Å}$ line (Carlsson et al. 1994).

In addition, we do not consider the effects of chromospheric and/or magnetic activity. To compensate for the former, we exclude from our fitting method emission lines due to chromospheric activity that are frequently seen in classical T Tauri and post T Tauri stars (described further in §4.1). We also note here that very strong lines — which are completely dominated by pressure broadening, a relatively poorly understood process — require special treatment to reproduce the line profile. Although the models include attempts to do this, it does not always work satisfactory. The resulting mismatches primarily affects lines from neutral metals that are highly abundant and very optically thick (such as K I and Na I). For less abundant neutral metals, such as Li I, the effects should be minimal.

4. SURFACE GRAVITIES AND EFFECTIVE TEMPERATURES

We derive surface gravities and effective temperatures, following the methodology of Mohanty et al. (2004), by fitting theoretical spectra to our observed spectra in small, $80\,\text{Å}$ wide, spectral regions that contain absorption lines or molecular bands that are highly sensitive to surface gravity and/or effective temperature.

4.1. *Modifications to the data*

To ensure our measurements would not be influenced by telluric absorption lines, or by stellar emission related to activity, we made some alterations to the observed spectra before fitting. For the telluric lines, we first used multi-epoch observations of one of our stars (β Pic) to identify the stronger atmospheric lines and determine their depths relative to the continuum. Next, for each spectrum, we marked a fixed spectral width of data points around the center of each telluric line as contaminated; these regions are ignored in all fits done below. We used widths of the marked regions that depended on the strength of the telluric line (as measured for β Pic): a region of $0.2\,\text{Å}$ was removed for relatively weak lines, which had a depth less than 80% of the continuum. Regions of $0.6\,\text{Å}$ were removed for line depths between 80% and 88%, while for the strongest, deeply saturated absorption lines, $1.0\,\text{Å}$ wide regions were removed.

As our sample consists of young stellar groups, many of the stars show signatures of activity, with relatively narrow chromospheric emission lines found in many of our targets, and strong and wide emission lines indicative of accretion in a few others (Jayawardhana et al. 2006; Scholz et al. 2007). The chromospheric activity causes emission features at a number of wavelengths, with the strengths and locations depending on spectral types and age (Eislöffel et al. 1990). To mitigate the effects of activity, we exclude $2.4\,\text{Å}$ regions around lines

TABLE 1
SPECTRAL REGIONS FITTED

Line ID	λ (Å)	$\Delta\lambda$ (Å)	T (K)	Sens.
Na I[a]	5 893	5 850–5 930	2 500–4 500	T, $\log g$
Fe I[a]	5 893, 5 898			
TiO[a]	5 847–6 058			T
VO[b]	7 851–7 973	7 900–7 980	4 000–6 500	T
CN[a,b]	7 916, 7 941, 7963			
Na I[b]	8 183, 8 195	8 150–8 230	2 500–3 000	$\log g$, T
TiO[a,b]	8 432, 8 442, 8 452	8 400–8 480	2 500–6 500	T
Fe I[b]	8 440, 8 468			
Ca II[a,b]	8 498, 8 542	8485–8565	2 500–6 500	T
VO[b]	8 521, 8 538			

NOTE. — A list of the spectral regions selected for our fitting method as described in §4.2 & §4.3. The first and second columns identify and locate spectral features within the chosen spectral range that show strong sensitivity to temperature and/or surface gravity. The third column lists the $80\,\text{Å}$ region that was selected in our fitting procedure. The fourth column indicates what range in effective temperature the selected region shows strong sensitivity to varying parameters and the fifth column indicates whether the region is more sensitive to effective temperature or surface gravity.
[a] Torres-Dodgen & Weaver (1993)[b] Kirkpatrick et al. (1991)

that frequently are seen in emission from classical T Tauri and post-T Tauri stars (Stahler & Palla 2005): He I at $5\,875.6\,\text{Å}$, Na I at $5\,890.0$ and $5\,895.9\,\text{Å}$, O I at $8\,446.5\,\text{Å}$, and Ca II at $8\,498.0$, $8\,542.1$ and $8\,662.1\,\text{Å}$.

Some stars also show signs of accretion, which leads to strong, wide emission features, potentially leading to less accurate fits. Since only three out of eleven η Cha and two out of 32 TWA members show signs of accretion (Jayawardhana et al. 2006), this will affect relatively few stars in the sample and in practice we do not find any effect of accretion on the uncertainties involved in constraining T_{eff}, $\log g$ and $\log N_{\text{Li}}$, except for the EW of one star (see §5.1). There are no known accretors in any of the older PMS groups investigated in this study.

4.2. *Selection of spectral regions*

We locate spectral regions that are strongly sensitive to surface gravity and temperature. Both Torres-Dodgen & Weaver (1993) and Kirkpatrick et al. (1991) have compiled lists of prominent absorption features useful for spectral classification of low-mass stars. For all, we checked whether our model spectra (see §3) indeed showed strong temperature and/or gravity sensitivity, and selected only those that did.

In general, the dependence of these features on our parameters is somewhat degenerate, as different T_{eff} and $\log g$ combinations can fit a given absorption feature equally well. As discussed in Mohanty et al. (2004), features that show contrasting dependence on gravity and temperature are needed to constrain the parameter space. Thus, we choose combinations of molecular absorption features like titanium oxide (TiO) and vanadium oxide (VO) with lines from neutral alkali elements, like K I, Na I and Mg I. This works well because, for neutral alkali elements, an increasing temperature can be compensated by increasing gravity, while the molecular absorption bands show less correlation between gravity and temperature. For instance, TiO bands in the vicinity of $7\,100\,\text{Å}$ are much more sensitive to temperature than to gravity, while the triple headed TiO bands in the range of $8\,440\,\text{Å}$ are more sensitive
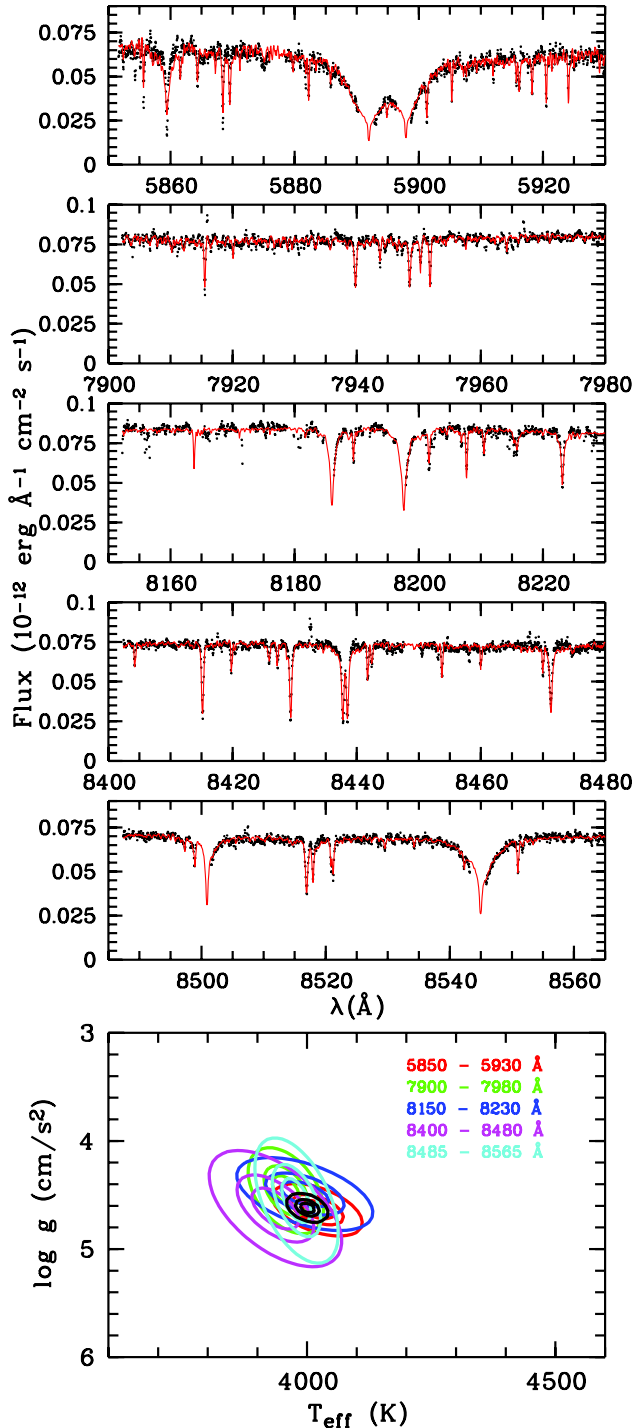
FIG. 1.— Spectral fits (solid red lines) to η Cha 10 (black dots), a K7 star, in the regions listed in Table 1. Quality of fit (χ^2) contours at 68.3,%, 95.4 % and 99.99 % confidence for each spectral window are shown in the bottom panel with each level given by $\chi^2_{\min} \times [1 + (2.30, 6.17, 18.4)/N_{\mathrm{dof}}]$, where N_{dof} is the degrees of freedom in the fit and $\chi^2_{\min}$ is the best-fit value. The summed χ^2 values for all spectral windows are represented by the tight solid black contours.

to gravity than to temperature. Examples of this dependence can be seen in the χ^2 contours shown in the bottom panels of Figs. 1 and 2. Of course, these dependencies change with temperature, and hence different sets of regions are best for different spectral types. In principle, one could choose to fit different regions in different temperature ranges, but

this risks (borne out in practise) that at the borders there are false jumps in parameters due to systematic problems with the models. Thus, we fit all regions for all stars, which gives very tight constraints on T_{eff} and $\log g$ for all spectral types (and more smoothly varying systematic offsets; see below). After investigating spectral fits of twelve individual regions collected from Torres-Dodgen & Weaver (1993) and Kirkpatrick et al. (1991), we settled on the five separate spectral regions listed in Table 1. Also listed is the effective temperature range where the features provide strong constraints, as well as whether these constraints are predominantly on T_{eff} and/or $\log g$.

We excluded regions which either tended to overestimate $\log g$ or provided $T_{\mathrm{eff}}/\log g$ values extremely offset from the majority of spectral regions. For instance, for many of the neutral metal lines, particularly K I at 7 665 and 7 699 Å, the best fits are at surface gravities much higher than are expected for late-type PMS stars. Since these lines are sensitive to gravity and generally fit the spectrum very well, the entire fit was very sensitive to the K I line. Due to this inconsistency between the line strengths in the atmospheric models and predicted surface gravity, this region and several others were not used. We note that we use other neutral metal lines such as Na I that could be flawed similarly. In practise though, these produced fits that were consistent with the other spectral regions investigated.

4.3. Fitting Methods

All spectra in our study with spectral types later than F5 (corresponding to about 6 500 K, the highest temperature for which we have models) were fitted to the synthetic spectra for each spectral window listed in Table 1. Prior to the fit, the synthetic spectra were convolved with a gaussian filter to match the observed resolution. The fit used a variant of the broadening-function formalism introduced by Rucinski (2002). In this formalism, a least-squares fit is made of the observed spectrum to a set of reference spectra that differ only in their velocity offset. This way, rotational broadening is automatically accounted for. The difference with the formalism of Rucinski is that the sum of the model spectra at various velocities is also multiplied with a polynomial, to account for not only the normalization, but also for small errors in the flux calibration. For our small wavelength regions, we found that a third-degree polynomial sufficed.

We note that our fitting method effectively introduces a relatively large number of parameters that are not of direct physical interest, viz., the line shape. Since these parameters might be covariant with some of the effects of temperature and/or gravity changes, the constraints on T_{eff} and $\log g$ we find are thus not as strong as might be possible if, e.g., instead we broadened the synthetic spectra with an analytic broadening model (with only the projected rotational velocity as parameter). In practice, however, the covariance is small, and our errors are clearly dominated by systematic mismatches between the models and the observations.

With the above least-squares fitting method, we fitted each of the five regions from each observed spectrum to 77 of the synthetic spectra, covering all seven values of $\log g$ (from 3.0 to 6.0 in steps of 0.5), and eleven temperatures in a range of 1 000 K around the effective temperature inferred from the object's spectral type (as listed in Tables 2–7; we used the temperature scale for dwarfs of Luhman & Rieke 1998). For new companions with unknown spectral types, initial estimates for the temperatures were found through trial and error.
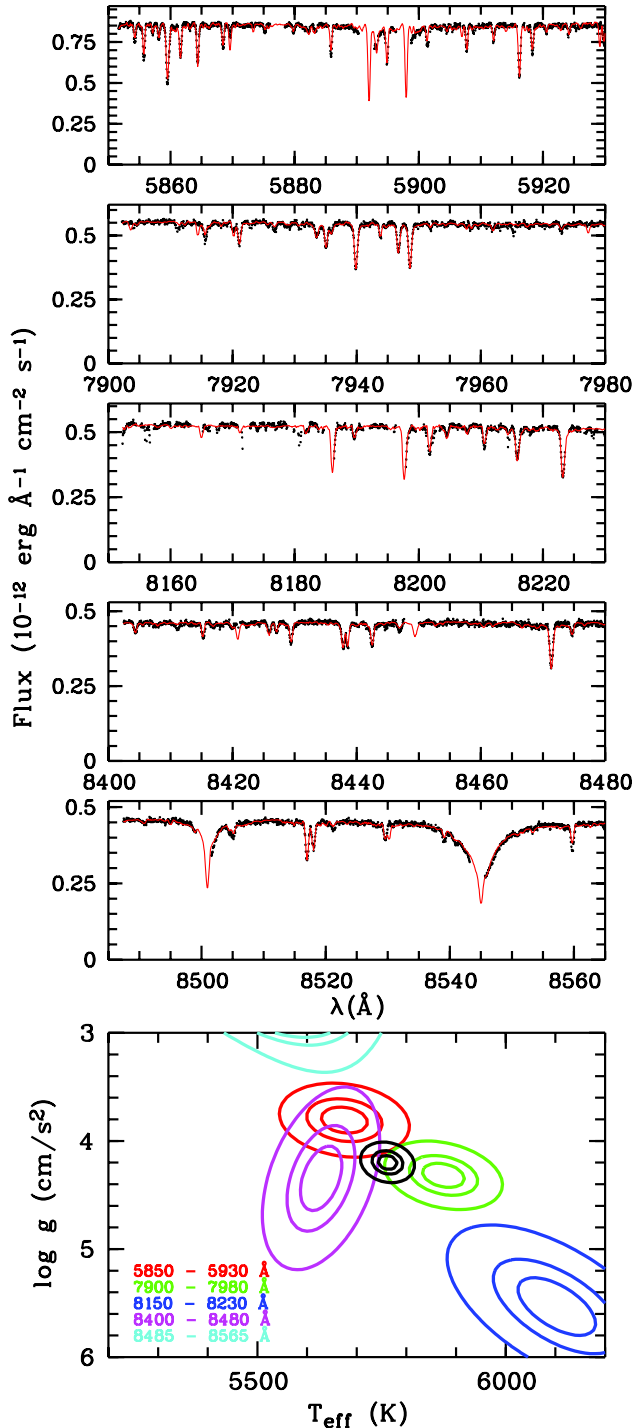
FIG. 2.— As Fig. 1, but for HIP 32235 (black dots), a G6V-type TUCHOR member.

for each spectrum, we interpolate in the 7 by 11 grid by determining the minimum of a two-dimensional parabola (of the form $a+bx+cy+dx^2+exy+fy^2$) fit to the sixteen grid points with the lowest values of χ^2.

4.4. *Examples*

In Fig. 1 and 2, we show our fits for one spectrum of each of the stars η Cha 10 and TUCHOR member HIP 33235. The gaps in the data in the panels centered on 5 890 and 8 525 Å are due to the removal of emission lines as discussed in §4.1. Similarly, on close inspection, one sees that multiple telluric lines have been removed from the 8 190 Å region.

Overall, the broadened models reproduce the observed spectra well. In detail, however, there are clear inconsistencies between the observed and synthetic spectra, apparent in many of the panels. In particular, a number of lines appear to be absent in the models, or are clearly too weak. We also found examples of the reverse in some other wavelength regions.

In the bottom panels of Figs. 1 and 2, the resulting 68.3 %, 95.4 % and 99.99 % confidence contours in the $T_{\rm eff}$-$\log g$ parameter space are shown, with levels set according to Press et al. (1992) at $\chi^2_{\rm min} \times [1 + (2.30, 6.17, 18.4)/N_{\rm dof}]$, where $N_{\rm dof}$ is the degrees of freedom in the fit and $\chi^2_{\rm min}$ is the best-fit value inferred from the parabolic fit. Contours are shown for each spectral window as well as for the total χ^2 values. For the different spectral regions, one notices the different covariances in $T_{\rm eff}$ and $\log g$, and how, by using a number of these sensitive regions, it is possible to constrain gravity and temperature precisely. Indeed, the contours for the summed χ^2 distribution (solid black contours) are extremely tight. We will see below that different spectra of the same star lead to similarly small scatter in the inferred temperature and gravity.

One also notices, in particular in Fig. 2, that the contours for the different regions are statistically inconsistent with each other, with differences of several 100 K in $T_{\rm eff}$ and up to 1 dex in $\log g$. These differences likely reflect systematic uncertainties in the models, similar to what we find for the resulting best-fit average values below.

4.5. *Results*

The best-fit model $T_{\rm eff}$ and $\log g$ with corresponding errors, for each star, including field stars, can be found in Tables 2–7. We consider two ways of estimating the associated uncertainties. First, we follow Press et al. (1992) and use the curvature of the best-fit two-dimensional parabola to the χ^2 values to find regions which are enclosed within a level of 68% confidence. Second, we consider the error in the mean between the results from different spectra of the same source taken at different epochs (e.g. the standard deviation divided by the square root of the number of observations taken).

For the temperatures, our statistical uncertainties are typically around 9 K, while the scatter derived from multiple observations of the same object is on average 11 K. For the surface gravities, our statistical uncertainties numbers are 0.02 dex on average, and the scatter derived from the error in the mean from multiple observations is about 0.03 dex. The above suggests the true intrinsic uncertainties ($\sigma_{\rm int}$) in our temperature and gravity measurements are very small, about 10 K and 0.05 dex for a single observation. We will see below, however, that systematic mismatches as a function of, e.g., spectral type, are much larger.

To determine combined constraints on $T_{\rm eff}$ and $\log g$ for a given spectrum, we add up the χ^2 values derived for the five regions. The results are similar to fitting the five regions together, except that our method leaves greater freedom for variations in continuum (which might be expected) or line shape (which would not). The difference with fitting the entire spectrum is that we have effectively ignored the parts of the spectrum that are either insensitive to $T_{\rm eff}$ and $\log g$ or where the models are shown to fit poorly to the observations.

For our final estimates of the best-fit values of $T_{\rm eff}$ and $\log g$
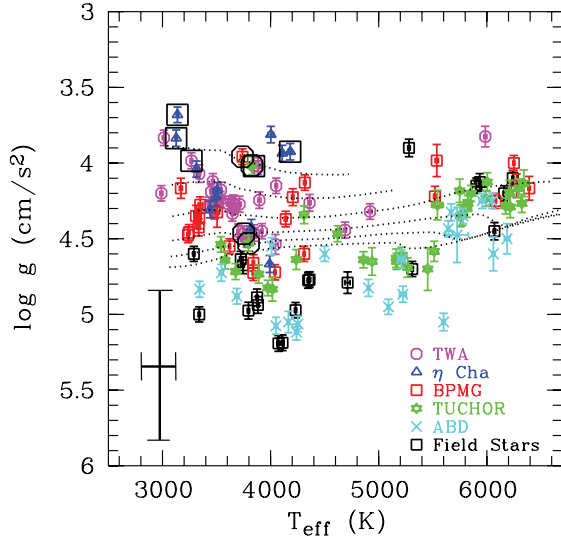
FIG. 3.— Surface gravity, $\log g$, as a function of effective temperature, $T_{\rm eff}$, for all five PMS groups, as well as field stars. PMS tracks from BCAH98 are overdrawn, with, from top to bottom, ages of 4, 8, 15, 25, 35, 45 and 150 Myr. We represent the external error in the plotted parameters for the ensemble in the bottom-left corner. It is evident that there are systematic problems with the values of $\log g$ derived from the models, particularly for $3500 < T_{\rm eff} < 4100\,$K. However, the relative ordering is clear: stars that are older, such as ABD and TUCHOR members, have higher surface gravities than younger stars. The ultrafast rotators and accretors in our sample are marked with circles and squares, respectively.
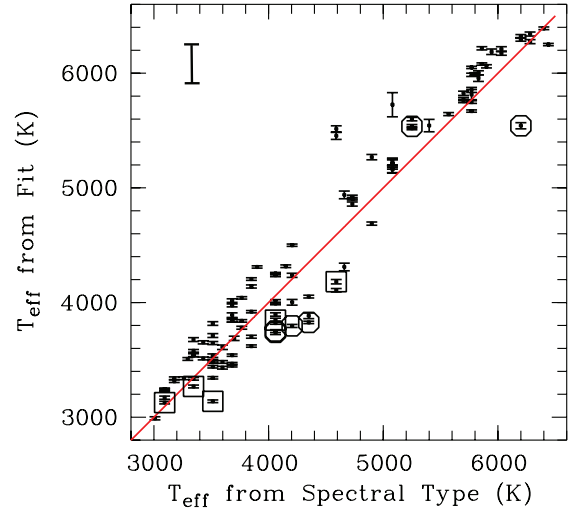

FIG. 4.— Comparison of the temperatures obtained from spectral fitting (see §4.3) with those derived from spectral types using the scale of Luhman & Rieke (1998). We represent the external error in the plotted parameters for the ensemble in the top left corner. The ultrafast rotators and accretors in our sample are marked with circles and squares, respectively.

In Fig. 3, we show the distribution of $\log g$ as a function of $T_{\rm eff}$ for each group as well as for the field stars observed. In addition, we draw isochrones from the BCAH98 PMS evolutionary models. One immediately sees there is a clear systematic problem in determining $\log g$ for stars with $3500 < T_{\rm eff} < 4100\,$K: $\log g$ increases with temperature from $3000\,$K to $4000\,$K, but at around $4000\,$K, it becomes almost 1 dex smaller, an unrealistic physical trend. The systematic differences in $\log g$ can result from a few effects. If the resolution of the model spectra is not much better than the observations before smoothing, line depths can be systematically off. In addition, stellar activity also introduces systematic errors, as has been found for young M-dwarfs, where the chromosphere feeds back into the photosphere (Fuhrmeister et al. 2005). This feedback is not incorporated into the model, and may lead to systematic errors of about 0.5 dex in $\log g$.

To evaluate the dependence of the fitted $T_{\rm eff}$ on $\log g$, we re-fit our spectra three more times using the same method described in §4.1, except with $\log g$ fixed to 4.0, 4.5 and 5.0. The change in $T_{\rm eff}$ across the surface gravity space is small in an absolute sense. Going from log g fixed at 4.0 to 4.5, the average change in temperature within our sample is $\Delta T_{\rm eff} = 71\,$K. It is slightly higher going from 4.5 to 5.0, with $\Delta T{\rm eff} = 124\,$K. Changes from $\log g = 4.0$ to 5.0, yield absolute average changes in $T_{\rm eff}$ of 162 K.

Thus, the external errors related to the models are much higher than the internal errors. Tables 2 to 7 list the best-fit surface gravities and temperatures with quoted errors representing the error in the mean of multi-epoch observations of the object. More conservatively, we consider our external errors to be 150 K in $T_{\rm eff}$ and 0.5 dex in $\log g$.

In Fig. 4, we compare our computed temperatures to those obtained by converting spectral types to effective temperatures using the temperature scale for dwarf-type stars of Luhman & Rieke (1998). Generally, the two scales are con-

sistent within the external errors just discussed, with the largest deviations show by the accretors (marked by squares) and ultrafast rotators (marked by circles, see also §5.4). In addition, most of the objects with $T_{\rm eff} > 5000\,$K, while individually consistent within the uncertainties, appear systematically to have fitted temperatures slightly greater than those inferred from spectral type, suggesting a small systematic error.

5. LITHIUM ABUNDANCES

We analyse lithium abundances using two independent methods. In one method, which follows previous work (Jeffries & Oliveira 2005), we measure the equivalent width (EW) of the 6 708 Å lithium absorption doublet for each spectrum. We use this measurement and the spectral types quoted in the literature to chronologically order the groups. The other method uses the best-fit model calculated in §4 to fit model spectra for various lithium abundances to regions surrounding the 6 104 and 6 708 Å lithium absorption features. As with our EW measurements, we chronologically order the groups. Further, we compare the observations with PMS models of BCAH98 and Siess et al. (2000) to see if the isochrone ages based on lithium abundances are consistent with other age determinations of the five nearby PMS groups in this study

5.1. *Lithium equivalent widths*

First, we use the EW of the 6 708 Å lithium doublet feature in each observed spectrum as an empirical measurement of the lithium abundance. To measure it, we interactively chose the edges of the lithium feature and the boundaries of sufficiently large regions around it to define the stellar continuum. We chose to consistently reject the lowest 15% of the flux points in the continuum region (corresponding to the deepest absorption features), so that we do not underestimate the continuum flux. We do not apply any correction for the 5 identified accretors in our sample, but find that veiling due to accretion can reduce the measured EW, as discussed briefly below.

The resulting mean EWs, averaged over all available spectra, are listed in Tables 2 to 6, with uncertainties being the error in the mean between multiple spectra. Fig. 5 displays the resulting EWs as a function of spectral type. From this
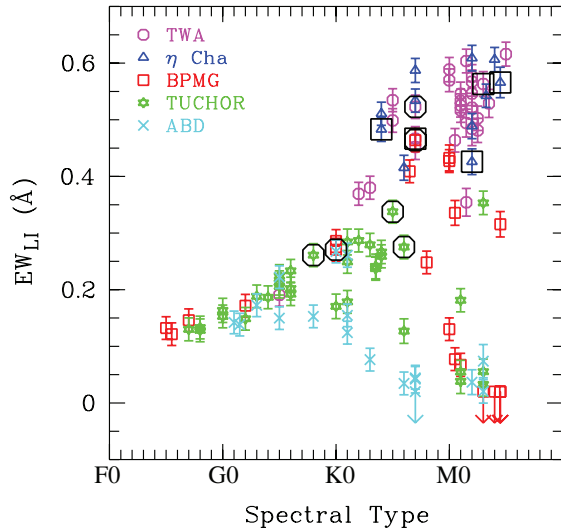
FIG. 5.— Equivalent width (EW) of the 6708 Å lithium line as a function of spectral type. Without depletion, the EW would increase with decreasing temperature, as is seen with the youngest two groups, TWA and η Cha. But in older groups lithium is being depleted, and the order, from youngest to oldest, is evident: BPMG, TUCHOR, and ABD. We identify the ultrafast rotators and accretors in our sample with black circles and squares, respectively.

purely empirical figure, the chronological order of the groups is evident: from oldest to youngest, they are ABD, TUCHOR, BPMG, TWA and η Cha. The same ordering was found by Zuckerman & Song (2004) from lithium EWs for a smaller sample of stars. Although some TWA members appear to be as young as those in η Cha, it is quite clear that no members are older than BPMG, contrary to the suggestion by Lawson & Crause (2005). (Note that we implicitly assume here the initial lithium abundance was the same for all groups. We return to this below.)

We identify the ultrafast rotators and accretors in our sample with black circles and squares, respectively. The EWs of the rotators in BPMG (red squares) and TUCHOR (green stars) stand out above the general trend for each group; we will return to this in §5.4. We also note that one accretor in η Cha, (η Cha 13) has a lithium EW that is lower than most objects at the same temperature ($\sim$ 3100 K) and age, but we will find below a lithium abundance near initial from the fits to the spectra of this star (see §5.2). This suggests the low estimate of the EW is related to the fact that it is accreting, either by its effect on the continuum level or alternatively, by us underestimating the temperature. Indeed, the latter may well play a role: from our spectral fit, we infer $T_{\rm eff} = 3139 \pm 96$ K, while that from its M2 spectral type, one would estimate $T_{\rm eff} = 3514$ K (Luhman & Rieke 1998). With the latter temperature, the object would match the trend much better. Because of the large accretion lines in the spectra, the models are a poor representation of the data throughout the regions selected for our fits. A higher temperature model is just a slightly worse fit to the observations.

5.2. Lithium Line Analysis

Using the average best-fit effective temperatures and surface gravities listed in Tables 2 to 7, synthetic spectra, varying in lithium abundance from $\log N_{\rm Li} = 0.0$ to 4.0 in steps of 0.5, are, for each spectrum, fitted to small spectral regions around the 6104 Å and 6708 Å lithium absorption lines. The fitting method is identical to the method outlined in §4.3. However, we constrain the minimization of the least-squares fit

in a slightly different manner.

Synthetic spectra of varying lithium abundance are fitted to 20 Å wide spectral regions – specifically 6095–6115 Å and 6695–6715 Å. The 6104 Å lithium triplet line is a weaker transition than the 6708 Å doublet line. It is also blended into the strong 6103 Å Ca II absorption line. As a result, the line is only detectable for high lithium abundance. Overall, we are not very sensitive to this line, detecting only a small change in χ^2 over the entire lithium abundance range. This is not the case with the stronger lithium doublet at 6708 Å, which is very sensitive to lithium abundance, and shows sharp transitions from good to bad in its least-squares fits. For high lithium abundances, however, the line saturates and without the 6104 Å line no good abundance estimates are possible.

In order to be able to treat all data uniformly, irrespective of lithium abundance, we proceeded as follows. First, we use the 6708 Å region, with its higher sensitivity, to determine the approximate abundance, and select the points with $\log N_{\rm Li}$ corresponding to the 4 lowest χ^2 values from the fit to this region. For both spectral regions, we then fit a 2nd order polynomial to the χ^2 for these 4 selected $\log N_{\rm Li}$. Next, we normalize both fitted polynomials by dividing by the minimum χ^2 value for each spectral region. The two normalized curves are then added together to give an average curve, and the minimum of this curve is what we take to be the best-fit $\log N_{\rm Li}$. Thus, in our procedure for determining the lithium abundances, we give equal weight to both regions, unlike the procedure outlined in §4.3, where we desired to keep the weight on the best fitted regions by summing the raw χ^2 values.

By way of example, we show, in Fig. 6, the spectral fits to the two lithium features for three stars with distinctly different lithium abundances. The resulting normalized χ^2 curves are shown in the bottom panel for each star. Averages of the best-fit $\log N_{\rm Li}$ for all stars can be found in Tables 2 to 7, with uncertainties representing the error in the mean between multi-epoch observations.

As discussed in §4.5, uncertainties in the model atmospheres lead to larger errors than the internal errors quoted in Tables 2 to 7. Thus, we also handle external errors for the lithium abundances with the same approach. We investigate changes in the fitted abundances by re-fitting the lithium lines to models with $T_{\rm eff}$ perturbed by ± 100 from the initial best-fit $T_{\rm eff}$ and also to models with $\log g$ also perturbed by ± 0.5 dex. We find that this parameters leads to changes in $\log N_{\rm Li}$ of 0.15 on average. We show this error on all relevant figures to indicate our estimate of the external uncertainties.

5.3. Ages from the lithium abundance versus temperature isochrones

As a PMS group ages, the lithium abundances of group members deplete as a function of luminosity and time (see §1). As with EWs in §5.1, we can order the groups in age using the relative depletion of members of different groups and by comparison with models, we can also determine absolute ages. Of course, the absolute ages will only be as good as the models. To get an idea of the associated uncertainty, we try both the models of BCAH98 and Siess et al. (2000).

In Fig. 7, we show the distribution of measured lithium abundance as a function of temperature for each of the groups in this study, as well as for the field stars (which should be fully depleted). As with the EWs in §5.1, it is easy to order the groups chronologically based on the lithium depletion distribution: from oldest to youngest, we again find the order
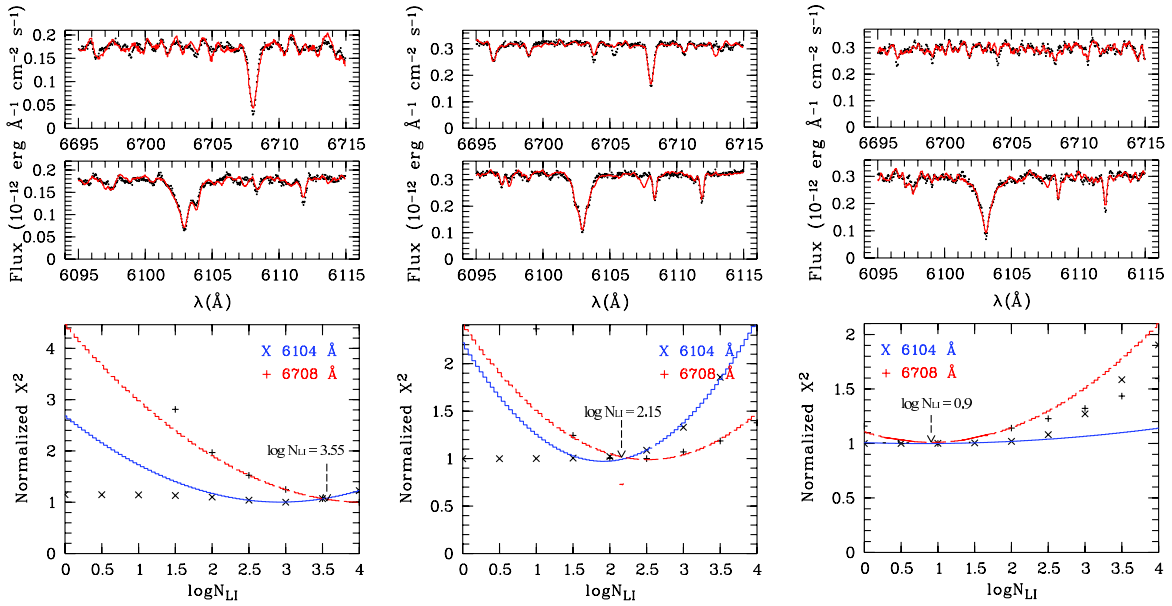
FIG. 6.— Examples of fitting the two lithium features to three stars (from left to right: TWA 02A (M2e), CD-60 416 in TUCHOR (K3/4) and GJ 3305 in BPMG (M0.5)). For each star, the top panel shows the fit to the strong 6 708 Å lithium doublet and the middle panel the fit to the much weaker 6 104 Å lithium line. The bottom panel shows the normalized χ^2 values for the abundances at which we had models, and the parabolic interpolations used to determine the best-fit abundances (which is taken to be at the minimum of the sum of these two curves; see §5.2).
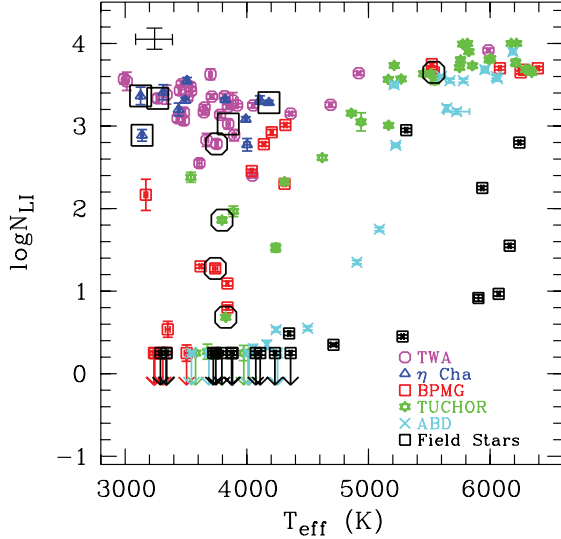

FIG. 7.— Lithium abundance derived by fitting the 6 104 Å and 6 708 Å spectral features as a function of temperature. We identify the ultrafast rotators and accretors in our sample with black circles and squares, respectively.

ABD, TUCHOR, BPMG, and then η Cha and TWA both at about the same age. It is also clear that the field stars are older than all of the PMS groups in this study.

In Fig. 8, the dependence of $\log N_{Li}$ on stellar T_{eff} is shown for each group individually, and a range of PMS isochrones from BCAH98 (solid lines) and Siess et al. (2000) (dashed lines). Both models use a convection mixing length of $\alpha_{MLT} = 1.9$ and are scaled to the initial lithium abundance. We chose an initial lithium abundance of $\log N_{Li} = 3.7$ to match the abundance we measured from our method (see §5.2) for the majority of undepleted stars in the entire sample. The inferred ages do depend on this choice, as well as the choice of model.

From Fig. 8, we can infer ages by eye for each group. We tried but decided not to use quantitative analysis, because it is apparent that the models do not reproduce the data to

enough accuracy, especially in the temperature range where the lithium abundances are most dependent on age. In general, we find that the models of BCAH98 fit the nature of the depletion slightly better for all of the groups, but that the ages derived are similar, apart from a small systematic offset (with BCAH98 giving slightly higher ages).

We find that a lithium depletion age of 12 ± 6 Myr for η Cha using the models of BCAH98 (12 ± 8 Myr using the Siess et al. (2000) models; hereafter given in parentheses), and and an age of 12 ± 8 Myr (12 ± 8 Myr) for TWA, consistent with dynamical expansion ages (Jilinski et al. 2005; de la Reza et al. 2006) and other age estimates also based on BCAH98 PMS models (Luhman & Steeghs 2004; Zuckerman & Song 2004; Barrado y Navascués 2006). For BPMG, we find an age of 21 ± 9 Myr (13 ± 5 Myr), which is in agreement with the estimate of 9–17 Myr from other methods (Zuckerman & Song 2004; Feigelson et al. 2006). It is slightly higher than its dynamical expansion age of 11.5 Myr from Ortega et al. (2002), but agrees with a different age based on lithium dating of 10–20 Myr recently found by Mamajek et al. (2007). For TUCHOR, we find an age of 27 ± 11 Myr (22 ± 10 Myr), which is consistent with all previous age estimates for this group (Zuckerman & Webb 2000; Stelzer & Neuhäuser 2000).

For ABD, we find that it is clearly older than TUCHOR and clearly younger than the field stars, however the age estimate from PMS models is poorly constrained. Although the field stars show more depletion than ABD, this is not predicted by the PMS isochrones; both models show no depletion after ~45 Myr for stars with $4\,000 < T_{eff} < 6\,000$ K. Until the PMS evolutionary models are improved, the best way to find an upper limit to the age of the ABD group would be to use the cool end of the LDB. This would require stars with spectral types later than M3 ($T_{eff} \lesssim 3\,300$ K), but, unfortunately, no such members are known in ABD. Within our present large uncertainties, our age estimate is consistent with both a younger estimate of 50 Myr based on Hα emission strength (Zuckerman et al. 2004), as well as an older one of

100–140 Myr from HR isochrones (Luhman et al. 2005) and dynamical expansion (Ortega et al. 2007).

We close with a number of notes. First, while the poor fit of the data to the models leads to rather large uncertainties on the ages, these should be considered overall shifts: the age ordering of the groups is secure. Second, an additional uncertainty in the derived ages is our choice of initial lithium abundance, of $\log N_{\mathrm{Li}} = 3.7$ based on our observations. Decreasing the initial lithium abundance to $\log N_{\mathrm{Li}} = 3.3$ (as used in Jeffries & Oliveira (2005)), predicts younger group ages by about 5 Myrs. On the other hand, using a higher initial lithium abundance of $\log N_{\mathrm{Li}} = 4.0$, yields ages larger by 5-10 Myrs. Third, we have ignored non-LTE effects in the lithium lines (§3). While our scatter is larger than the predicted effects, the systematic changes with temperature and abundance will lead to additional systematic age differences. It also may be the underlying reason for our need for a relatively high initial abundance: Carlsson et al. (1994) found that around 6000 K, the correction for the 6708 line is about −0.3 dex, which would imply initial abundances more in line with expectations (at these temperatures, the 6104 Å line is very weak and contributes little to our fits.

5.4. *The Effect of Rotation on Lithium Depletion*

We examine the effect of stellar rotation on lithium depletion using projected rotational velocities found previously from our observations (Jayawardhana et al. 2006; Scholz et al. 2007). In Fig. 8, we identify ultrafast rotators as those stars that have $v \sin i > 70 \, \mathrm{km \, s^{-1}}$. One member (TWA 6) from TWA, two members (PZ Tel, CD 64d1208) of BPMG and three members (CD 53 544, HIP 108422, HIP 2729) of TUCHOR are identified as ultrafast rotators. In three of the cooler stars ($T_{\mathrm{eff}} \sim 3800 \, \mathrm{K}$), CD 64d1208, CD 53 544 and HIP 2729 , the lithium EWs are noticeably higher, and the derived abundances larger, than the trend in lithium depletion for the entire group. The correlation between fast rotation and slower lithium depletion has also been seen previously in a sample of weak-line T Tauri stars (Martín et al. 1994) and in the 115 Myr Pleiades cluster (Soderblom et al. 1993; García López et al. 1994). It may be related to rapidly rotating stars being relatively cooler as the rapid rotation inhibits convection (Chabrier et al. 2007). This alternative view is supported by the location of the rotators in Fig. 4. It is evident that the T_{eff} derived for these rotators is 100–300 K cooler than the temperature derived from their spectral types. It may be that the presence of a colder equatorial region and a hotter polar one affects the model fits differently than the spectral typing.

However, the trend that lithium depletion is slowed down by rotation is not seen in all of our ultrafast rotators. The relatively slower rotators PZ Tel ($v \sin i = 77.5 \, \mathrm{km \, s^{-1}}$) and TWA 6 ($v \sin i = 79.5 \, \mathrm{km \, s^{-1}}$) have lithium abundances comparable to other members in their groups. For our faster rotator, HIP 108422 ($v \sin i = 139.8 \, \mathrm{km \, s^{-1}}$), the spectrum is so strongly broadened that our fitting method does a poor job and we see no change in the quality of fit for varying lithium abundances. For this, reason, we do not quote an abundance for this object, but do note, however, that the equivalent width measured is consistent with other group members.

5.5. *Notes on Individual Systems*

BD 17°6128 – This binary system from BPMG consists of a K7 primary with $T_{\mathrm{eff}} = 4\,140 \, \mathrm{K}$ and $\log N_{\mathrm{Li}} = 2.78$ and a lithium depleted secondary of $T_{\mathrm{eff}} = 3\,350 \, \mathrm{K}$ and $\log N_{\mathrm{Li}} = 0.54$. This system is unique to our sample as it is the only case of the cool end of the LDB in effect within a binary, and provides a precise, if model dependent, age of the system. Using the models from BCAH98, an age of 15–50 Myr is predicted, consistent with the age we inferred for BPMG as a group.

GSC 08056-0482 – The measured $\log N_{\mathrm{Li}}$ for TUCHOR member GSC 08056-0482 is much higher than expected for a $\sim 30 \, \mathrm{Myr}$ old, M3 dwarf. Indeed, another M3 star in the younger BPMG, GSC 08491-1194, has an abundance over two orders of magnitude smaller (consistent with models at $\sim 20 \, \mathrm{Myr}$). With a modest $v \sin i$ of $34.2 \, \mathrm{km \, s^{-1}}$ (Jayawardhana et al. 2006), rotation does not explain the high lithium abundance. As pointed out already by previous authors (see Table 3 of Zuckerman & Song 2004), the lithium abundance suggests that GSC 08056-0482 is likely not a member of TUCHOR, but a star slightly older than TWA and η Cha, but definitely younger than BPMG.

6. SUMMARY AND OUTLOOK

We have measured effective temperatures, surface gravities, lithium equivalent widths and lithium abundances for 121 low-mass PMS stars from five nearby, PMS groups ranging in age from 8–125 Myr by performing least-squares fits of high resolution spectra to synthetic spectra created from PHOENIX model atmospheres (Hauschildt & Baron 1999). To investigate the reliability of our measurements we compare the derived T_{eff} and $\log g$ with isochrones from PMS evolutionary models (BCAH98) as well as temperatures derived from spectral types.

Isochrones from PMS models for $\log N_{\mathrm{Li}}$ as a function of T_{eff} are visually compared to the observed distribution. We find agreement between ages derived from PMS isochrones of BCAH98 and Siess et al. (2000) to ages calculated from other methods such as dynamical expansion ages. We find that η Cha and TWA have ages of $12 \pm 6 \, \mathrm{Myr}$ and $12 \pm 8 \, \mathrm{Myr}$, respectively. BPMG has an age of $21 \pm 9 \, \mathrm{Myr}$, and TUCHOR has an age of $27 \pm 11 \, \mathrm{Myr}$. We can only constrain a tight lower limit for ABD, with an age greater than 45 Myr, since, according to the PMS models, there is no more lithium depletion after $\sim 45 \, \mathrm{Myr}$ for stars with $4\,000 < T_{\mathrm{eff}} < 6\,000 \, \mathrm{K}$. However, the halting of lithium depletion at this age and temperature is inconsistent with observations of radial velocity standards which demonstrate more depletion than the ABD group and the model predictions. Finally, we find that some of the ultrafast rotators in our sample have significantly less lithium depletion than other stars in the same group at the same temperature.

The consistent determination of T_{eff} and $\log g$ between multiple epochs ($\sigma_T \simeq 10 \, \mathrm{K}$, $\sigma_{\log g} \simeq 0.05 \, \mathrm{dex}$) means that, in principle, we should be able to constrain those parameters with this precision. As revealed by Fig. 3, however, there is an apparent systematic offset between the $\log g$ inferred from model spectra and $\log g$ expected from models of stellar evolution (§4.5). To account for these offsets, we introduce rough conservative external errors by examining how the measured parameters depend on each other. We find that the systematic errors in $\log g$ of 0.5 dex lead to systematic errors of 100 K in our ability to constrain the T_{eff}. These external errors, similarly lead to offsets in the measured lithium abundances of 0.15 dex.

The small internal errors that we have measured imply that currently our accuracy is limited by the models. With further improvements in the atmospheric models, there is a potential
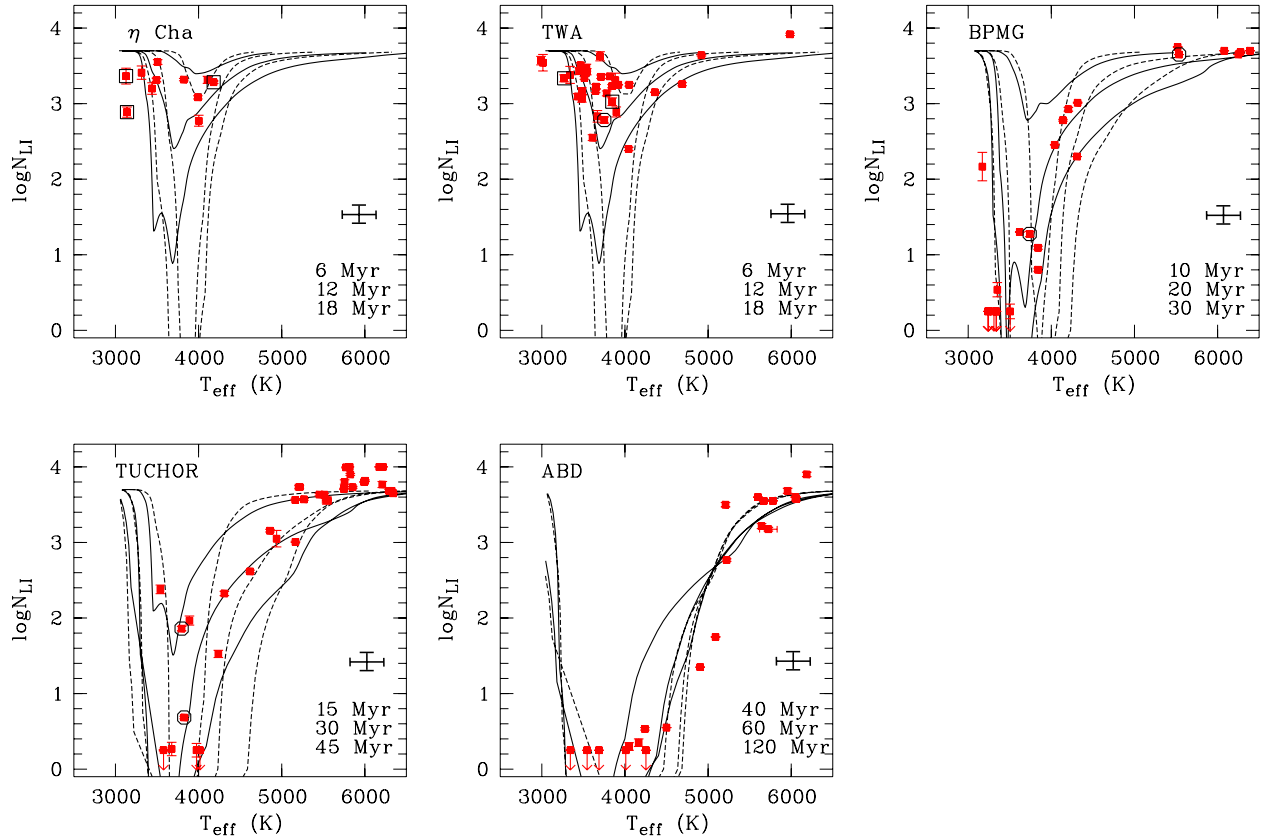
10

FIG. 8.— Lithium abundances derived from fits to the spectra as a function of temperature for each group. Overdrawn are predictions from the evolutionary models of BCAH98 (solid line) and Siess et al. (2000) (dashed line) as indicated by the ages in the bottom-right corner of each plots. Above the ages, external errors are shown. In addition, the ultrafast rotators are identified by black circle outlines, and accretors are identified by black square outlines.

of comparing $T_{\rm eff}$ and $\log g$ directly to evolutionary models, thereby finding an age constraint independent of other estimators, such as color-magnitude diagram or lithium depletion boundary fitting. Our data set would be well-suited for use with such future improved models. Another use of our data set would be to derive both overall metallicity and abundances for individual elements. While we do not believe this would affect our derived temperatures, etc., to a significant degree, it may be interesting to see how uniform the abundances are within (and between) groups, and whether there is any dependence on binarity, etc.

We thank the referee for an excellent and thorough review, which helped to improve our manuscript greatly. We also

REFERENCES

Asplund, M., Grevesse, N., & Sauval, A. J. 2005, Cosmic Abundances as Records of Stellar Evolution and Nucleosynthesis, 336, 25
Baraffe, I., Chabrier, G., Allard, F., & Hauschildt, P. H. 1998, A&A, 337, 403
Barrado y Navascués, D., Stauffer, J. R., & Patten, B. M. 1999, ApJ, 522, L53
Barrado y Navascués, D., Stauffer, J. R., & Jayawardhana, R. 2004, ApJ, 614, 386
Barrado y Navascués, D. 2006, A&A, 459, 511
Bildsten, L., Brown, E. F., Matzner, C. D., & Ushomirsky, G. 1997, ApJ, 482, 442
Chabrier, G., Gallardo, J., & Baraffe, I. 2007, A&A, 472, L17
Carlsson, M., Rutten, R. J., Bruls, J. H. M. J., & Shchukina, N. G. 1994, A&A, 288, 860
de la Reza, R., Jilinski, E., & Ortega, V. G. 2006, AJ, 131, 2609
Eislöffel, J., Solf, J., & Boehm, K. H. 1990, A&A, 237, 369
Feigelson, E. D., Lawson, W. A., Stark, M., Townsley, L., & Garmire, G. P. 2006, AJ, 131, 1730

Fuhrmeister, B., Schmitt, J. H. M. M., & Hauschildt, P. H. 2005, A&A, 439, 1137
García López, R. J., Rebolo, R., & Martín, E. L. 1994, A&A, 282, 518
Hauschildt, P. H. & Baron, E. 1999, Journal of Computational and Applied Mathematics, 109, 41
Jayawardhana, R., Coffey, J., Scholz, A., Brandeker, A., & van Kerkwijk, M. H. 2006, ApJ, 648, 1206
Jeffries, R. D., & Oliveira, J. M. 2005, MNRAS, 358, 13
Jilinski, E., Ortega, V. G., & de la Reza, R. 2005, ApJ, 619, 945
Kirkpatrick, J. D., Henry, T. J., & McCarthy, D. W., Jr. 1991, ApJS, 77, 417
Kučinskas, A., Hauschildt, P. H., Ludwig, H.-G., Brott, I., Vansevičius, V., Lindegren, L., Tanabé, T., & Allard, F. 2005, A&A, 442, 281
Kučinskas, A., Hauschildt, P. H., Brott, I., Vansevičius, V., Lindegren, L., Tanabé, T., & Allard, F. 2006, A&A, 452, 1021
Lawson, W. A., & Crause, L. A. 2005, MNRAS, 357, 139
Ludwig, H.-G., Allard, F., & Hauschildt, P. H. 2006, A&A, 459, 599
Luhman, K. L., & Rieke, G. H. 1998, ApJ, 497, 354

Luhman, K. L., Stauffer, J. R., & Mamajek, E. E. 2005, ApJ, 628, L69

Luhman, K. L., & Steeghs, D. 2004, ApJ, 609, 917

Makarov, V. V., Gaume, R. A., & Andrievsky, S. M. 2005, MNRAS, 362, 1109

Mamajek, E. E., Lawson, W. A., & Feigelson, E. D. 1999, ApJ, 516, L77

Mamajek, E. E., Barrado y Navascués, D., Randich, S., Jensen, E. L. N., Young, P. A., Miglio, A., & Barnes, S. A. 2007, ArXiv Astrophysics e-prints, arXiv:astro-ph/0702074

Martín, E.L., Rebolo, R., Magazzù, A. & Pavlenko, Ya.V. 1994, A&A, 282, 503

Mathieu, R. D., Baraffe, I., Simon, M., Stassun, K. G., & White, R. 2007, Protostars and Planets V, 411

Mohanty, S., Basri, G., Jayawardhana, R., Allard, F., Hauschildt, P., & Ardila, D. 2004, ApJ, 609, 854

Ortega, V. G., de la Reza, R., Jilinski, E., & Bazzanella, B. 2002, ApJ, 575, L75

Ortega, V. G., Jilinski, E., de la Reza, R., & Bazzanella, B. 2007, ArXiv Astrophysics e-prints, arXiv:astro-ph/0702315

Palla, F., & Stahler, S. W. 1999, ApJ, 525, 772

Press, W. H., Teukolsky, S. A., Vetterling, W. T., & Flannery, B. P. 1992, Cambridge: University Press, |c1992, 2nd ed.,

Rucinski, S. M. 2002, AJ, 124, 1746

Scholz, A., Coffey, J., Brandeker, A., & Jayawardhana, R. 2007, ArXiv e-prints, 704, arXiv:0704.3266

Siess, L., Dufour, E., & Forestini, M. 2000, A&A, 358, 593

Soderblom, D. R., Jones, B. F., Balachandran, S., Stauffer, J. R., Duncan, D. K., Fedele, S. B., & Hudon, J. D. 1993, AJ, 106, 1059

Song, I., Zuckerman, B., & Bessell, M. S. 2003, ApJ, 599, 342

Stahler, S. W., & Palla, F. 2005, The Formation of Stars, by Steven W. Stahler, Francesco Palla, pp. 865. ISBN 3-527-40559-3. Wiley-VCH , January 2005.,

Stassun, K. G., Mathieu, R. D., Vaz, L. P. R., Stroud, N., & Vrba, F. J. 2004, ApJS, 151, 357

Stauffer, J. R., Schultz, G., & Kirkpatrick, J. D. 1998, ApJ, 499, L199

Stauffer, J. R., et al. 1999, ApJ, 527, 219

Stelzer, B., & Neuhäuser, R. 2000, A&A, 361, 581

Torres, C. A. O., da Silva, L., Quast, G. R., de la Reza, R., & Jilinski, E. 2000, AJ, 120, 1410

Torres-Dodgen, A. V., & Weaver, W. B. 1993, PASP, 105, 693

Zapatero Osorio, M. R., Béjar, V. J. S., Pavlenko, Y., Rebolo, R., Allende Prieto, C., Martín, E. L., & García López, R. J. 2002, A&A, 384, 937

Zuckerman, B., & Webb, R. A. 2000, ApJ, 535, 959

Zuckerman, B., Song, I., Bessell, M. S., & Webb, R. A. 2001, ApJ, 562, L87

Zuckerman, B., & Song, I. 2004, ARA&A, 42, 685

Zuckerman, B., Song, I., & Bessell, M. S. 2004, ApJ, 613, L65

TABLE 2
RESULTS FOR STARS IN TW HYDRAE

Object ID	Sp.T.	# Obs.	EW$_{6708}$ (Å)	T_{eff} (K)	$\log g$	$\log N_{\text{Li}}$
TWA 1	K7e[a]	5	0.467 ± 0.021	3847 ± 16	4.02 ± 0.07	3.03 ± 0.05
TWA 2A	M2e[b]	5	0.567 ± 0.021	3712 ± 17	4.27 ± 0.05	3.36 ± 0.03
TWA 3A	M3e[b]	5	0.563 ± 0.022	3268 ± 12	3.98 ± 0.05	3.34 ± 0.05
TWA 3B	M3.5[b]	5	0.529 ± 0.025	3340 ± 13	4.07 ± 0.06	3.38 ± 0.11
TWA 4AN		4	0.359 ± 0.020	4045 ± 24	4.54 ± 0.07	2.40 ± 0.03
TWA 4AS		4	0.442 ± 0.020	4360 ± 14	4.26 ± 0.06	3.15 ± 0.02
TWA 5A	M1.5[b]	5	0.604 ± 0.021	3432 ± 12	4.28 ± 0.05	3.09 ± 0.04
TWA 6	K7[a]	5	0.523 ± 0.021	3751 ± 12	4.47 ± 0.05	2.78 ± 0.04
TWA 7	M1[a]	5	0.546 ± 0.021	3541 ± 10	4.18 ± 0.05	3.42 ± 0.05
TWA 8A	M2[a]	5	0.546 ± 0.021	3537 ± 15	4.24 ± 0.05	3.47 ± 0.05
TWA 8B		5	0.575 ± 0.026	3013 ± 15	3.83 ± 0.05	3.54 ± 0.11
TWA 9A	K5[a]	5	0.535 ± 0.020	4052 ± 12	4.15 ± 0.05	3.25 ± 0.03
TWA 9B	M1[a]	5	0.517 ± 0.021	3450 ± 12	4.19 ± 0.05	3.43 ± 0.05
TWA 10	M2.5[a]	5	0.481 ± 0.021	3512 ± 12	4.24 ± 0.05	3.34 ± 0.03
TWA 11B	M2.5[b]	5	0.503 ± 0.022	3653 ± 14	4.26 ± 0.05	3.22 ± 0.03
TWA 12	M2[b]	5	0.521 ± 0.020	3647 ± 13	4.33 ± 0.05	3.17 ± 0.03
TWA 13A	M1e[b]	5	0.533 ± 0.021	3845 ± 16	4.46 ± 0.05	3.23 ± 0.03
TWA 13B	M2e[b]	5	0.577 ± 0.021	3817 ± 16	4.47 ± 0.05	3.36 ± 0.03
TWA 14	M0[b]	5	0.589 ± 0.021	3701 ± 13	4.45 ± 0.05	3.63 ± 0.06
TWA 15A	M1.5[b]	5	0.494 ± 0.025	3482 ± 12	4.32 ± 0.05	3.07 ± 0.05
TWA 15B	M2[b]	5	0.484 ± 0.030	3483 ± 12	4.30 ± 0.06	3.16 ± 0.05
TWA 16	M1.5[b]	5	0.354 ± 0.024	3610 ± 20	4.27 ± 0.05	2.55 ± 0.04
TWA 17	K5[b]	5	0.499 ± 0.021	3884 ± 25	4.02 ± 0.06	3.31 ± 0.10
TWA 18	M0.5[b]	5	0.464 ± 0.021	3780 ± 13	4.50 ± 0.06	3.14 ± 0.04
TWA 19A	G5[a]	5	0.191 ± 0.020	5986 ± 14	3.83 ± 0.07	3.92 ± 0.03
TWA 19B	K7[b]	5	0.452 ± 0.022	3896 ± 15	4.24 ± 0.05	2.89 ± 0.07
TWA 21	K3/4[a]	5	0.369 ± 0.020	4689 ± 14	4.44 ± 0.05	3.26 ± 0.03
TWA 22	M5[a]	5	0.616 ± 0.021	2990 ± 13	4.20 ± 0.05	3.57 ± 0.06
TWA 23	M1[a]	5	0.525 ± 0.020	3466 ± 12	4.12 ± 0.05	3.51 ± 0.04
TWA 24N		5	0.438 ± 0.032	3669 ± 15	4.28 ± 0.06	2.83 ± 0.08
TWA 24S	K3[a]	5	0.380 ± 0.020	4920 ± 16	4.32 ± 0.05	3.64 ± 0.02
TWA 25	M0[a]	1	0.570 ± 0.020	3920 ± 10	4.45 ± 0.05	3.25 ± 0.02

NOTE. — all uncertainties are internal, derived from the scatter of fitted values from individual spectra from the mean. The external uncertainties are much larger (see §4.5).
[a] Zuckerman & Song (2004) [b] de la Reza et al. (2006)

TABLE 3
RESULTS FOR STARS IN η CHAMAELEONTIS

Object ID	Sp.T.	# Obs.	EW$_{6708}$ (Å)	T_{eff} (K)	$\log g$	$\log N_{\text{Li}}$
η Cha 1	K4[a]	5	0.511 ± 0.020	4107 ± 15	3.94 ± 0.05	3.31 ± 0.05
η Cha 3	M3.25[b]	5	0.542 ± 0.021	3508 ± 12	4.18 ± 0.05	3.55 ± 0.04
η Cha 4	K7[a]	5	0.587 ± 0.021	3822 ± 11	4.43 ± 0.05	3.32 ± 0.03
η Cha 5	M4[b]	5	0.606 ± 0.021	3314 ± 11	4.04 ± 0.05	3.41 ± 0.09
η Cha 6	M2[a]	4	0.489 ± 0.022	3492 ± 11	4.22 ± 0.06	3.31 ± 0.03
η Cha 7	K6[b]	5	0.415 ± 0.022	4002 ± 25	3.81 ± 0.05	2.77 ± 0.08
η Cha 9	M4.5[a]	5	0.566 ± 0.027	3127 ± 11	3.84 ± 0.05	3.36 ± 0.11
η Cha 10	K7[a]	5	0.534 ± 0.021	3992 ± 11	4.67 ± 0.06	3.08 ± 0.03
η Cha 11	K4[a]	5	0.483 ± 0.021	4182 ± 19	3.92 ± 0.05	3.28 ± 0.03
η Cha 12	M2[a]	5	0.609 ± 0.023	3440 ± 11	4.31 ± 0.06	3.20 ± 0.08
η Cha 13	M2[a]	5	0.426 ± 0.023	3139 ± 11	3.68 ± 0.05	2.89 ± 0.07

NOTE. — all uncertainties are internal, derived from the scatter of fitted values from individual spectra from the mean. The external uncertainties are much larger (see §4.5).
[a] Zuckerman & Song (2004) [b] Luhman & Steeghs (2004)

TABLE 4
RESULTS FOR STARS IN THE β PICTORIS MOVING GROUP (BPMG)

Object ID	Sp.T.	# Obs.	EW$_{6708}$ (Å)	T_{eff} (K)	$\log g$	$\log N_{\text{Li}}$
AO Men	K6/7	5	0.409 ± 0.020	4317 ± 12	4.13 ± 0.05	3.01 ± 0.02
AU Mic	M1e	5	0.067 ± 0.020	3841 ± 11	4.66 ± 0.05	0.80 ± 0.03
BD -17 6128A	K7e/M0	5	0.427 ± 0.020	4140 ± 13	4.37 ± 0.05	2.78 ± 0.02
BD -17 6128B		4	0.051 ± 0.035	3350 ± 19	4.28 ± 0.05	0.54 ± 0.10
CD -64 1208	K7	5	0.464 ± 0.021	3740 ± 19	3.96 ± 0.05	1.27 ± 0.04
GJ 3305	M0.5	5	0.077 ± 0.020	3840 ± 11	4.72 ± 0.05	1.09 ± 0.03
GJ 799N	M4.5e	5	0.020 ± 0.020	3237 ± 10	4.47 ± 0.05	0.25 ± 0.02
GJ 799S	M4.5e	5	0.020 ± 0.021	3244 ± 11	4.46 ± 0.05	0.25 ± 0.02
HD 164249B		4	0.075 ± 0.029	3505 ± 18	4.32 ± 0.10	0.25 ± 0.10
HD 181327	F5.5	5	0.122 ± 0.020	6392 ± 11	4.17 ± 0.08	3.70 ± 0.02
HD 35850	F7	5	0.146 ± 0.020	6275 ± 18	4.15 ± 0.08	3.68 ± 0.02
HIP 10679	G2V	1	0.172 ± 0.020	6080 ± 10	4.25 ± 0.05	3.70 ± 0.02
HIP 10680	F5V	1	0.132 ± 0.020	6250 ± 10	4.00 ± 0.05	3.65 ± 0.02
HIP 112312A	M4e	3	0.020 ± 0.020	3340 ± 12	4.37 ± 0.07	0.25 ± 0.02
HIP 112312B	M4.5	3	0.315 ± 0.022	3170 ± 14	4.17 ± 0.07	2.17 ± 0.19
HIP 11437A	K8	1	0.248 ± 0.020	4310 ± 10	4.60 ± 0.05	2.30 ± 0.02
HIP 11437B	M0	1	0.130 ± 0.020	3620 ± 10	4.55 ± 0.05	1.30 ± 0.02
HIP 12545	M0	2	0.433 ± 0.023	4205 ± 11	4.22 ± 0.06	2.92 ± 0.03
HIP 23309	M5	5	0.336 ± 0.022	4041 ± 10	4.72 ± 0.05	2.46 ± 0.02
HIP 23418N	M3V	2	0.020 ± 0.021	3335 ± 11	4.43 ± 0.06	0.25 ± 0.02
HIP 23418S		2	0.020 ± 0.022	3310 ± 14	4.35 ± 0.07	0.25 ± 0.02
PZ Tel	K0Vp	5	0.271 ± 0.020	5537 ± 15	3.98 ± 0.11	3.65 ± 0.02
V343 Nor	K0V	5	0.286 ± 0.020	5520 ± 13	4.22 ± 0.07	3.75 ± 0.02

NOTE. — all uncertainties are internal, derived from the scatter of fitted values from individual spectra from the mean. The external uncertainties are much larger (see §4.5). All spectral types from Zuckerman & Song (2004)

TABLE 5
RESULTS FOR STARS IN TUCANAE–HOROLOGIUM (TUCHOR)

Object ID	Sp.T.	# Obs.	EW$_{6708}$ (Å)	$T_{\rm eff}$ (K)	$\log g$	$\log N_{\rm Li}$
CD -53 544	K6Ve	5	0.275 ± 0.021	3796 ± 13	4.53 ± 0.05	1.86 ± 0.04
CD -60 416	K3/4	5	0.237 ± 0.021	4310 ± 33	4.34 ± 0.06	2.33 ± 0.03
CPD -64 120	K1Ve	5	0.284 ± 0.023	5212 ± 48	4.61 ± 0.05	3.73 ± 0.03
GSC 8056-0482	M3Ve	5	0.353 ± 0.021	3541 ± 13	4.54 ± 0.05	2.38 ± 0.06
GSC 8491-1194	M3Ve	5	0.033 ± 0.021	3578 ± 12	4.64 ± 0.06	0.25 ± 0.02
GSC 8497-0995	K6Ve	4	0.127 ± 0.022	4238 ± 18	4.64 ± 0.07	1.52 ± 0.05
HD 13183	G5V	5	0.205 ± 0.020	5854 ± 22	4.20 ± 0.05	3.73 ± 0.02
HD 13246	F8V	5	0.133 ± 0.020	6292 ± 13	4.17 ± 0.06	3.68 ± 0.03
HD 8558	G6V	5	0.192 ± 0.020	5825 ± 19	4.27 ± 0.05	3.90 ± 0.02
HD 9054	K1V	5	0.178 ± 0.020	5165 ± 35	4.65 ± 0.05	3.01 ± 0.02
HIP 105388	G5V	5	0.224 ± 0.020	5748 ± 11	4.18 ± 0.08	3.71 ± 0.02
HIP 105404	K0V	5	0.171 ± 0.022	5543 ± 54	4.28 ± 0.10	3.56 ± 0.05
HIP 107345	M1	5	0.055 ± 0.021	3975 ± 13	4.82 ± 0.05	0.25 ± 0.09
HIP 108422	G8V	5	0.261 ± 0.020	5541 ± 27	3.99 ± 0.07	N/A[a]
HIP 1113	G6V	3	0.202 ± 0.020	5757 ± 13	4.35 ± 0.07	3.80 ± 0.04
HIP 116748N		3	0.218 ± 0.020	4620 ± 10	4.47 ± 0.05	2.62 ± 0.03
HIP 116749S	G51V	3	0.212 ± 0.021	5813 ± 44	4.30 ± 0.06	4.00 ± 0.02
HIP 1481	F8	3	0.128 ± 0.020	6323 ± 13	4.27 ± 0.06	3.68 ± 0.03
HIP 16853	G2V	5	0.149 ± 0.020	6217 ± 14	4.29 ± 0.07	4.00 ± 0.02
HIP 1910	M1	3	0.181 ± 0.020	3890 ± 20	4.73 ± 0.06	1.97 ± 0.06
HIP 1993	M1	3	0.038 ± 0.022	4017 ± 16	4.83 ± 0.08	0.25 ± 0.02
HIP 21632	G3V	5	0.188 ± 0.020	6003 ± 18	4.12 ± 0.06	3.82 ± 0.02
HIP 22295	F7V	5	0.130 ± 0.020	6342 ± 17	4.13 ± 0.09	3.65 ± 0.02
HIP 2729	K5V	3	0.338 ± 0.020	3827 ± 11	4.64 ± 0.05	0.68 ± 0.03
HIP 30030	G0	5	0.163 ± 0.021	6210 ± 21	4.19 ± 0.08	3.77 ± 0.04
HIP 30034	K2V	5	0.287 ± 0.020	5268 ± 23	4.69 ± 0.06	3.57 ± 0.02
HIP 32235	G6V	5	0.233 ± 0.020	5774 ± 13	4.34 ± 0.07	3.99 ± 0.02
HIP 33737	K3V	5	0.279 ± 0.020	4859 ± 18	4.64 ± 0.05	3.16 ± 0.03
HIP 3556	M3	3	0.055 ± 0.022	3677 ± 17	4.72 ± 0.05	0.27 ± 0.09
HIP 490	G0V	3	0.153 ± 0.020	6173 ± 17	4.28 ± 0.05	4.00 ± 0.02
HIP 9141	G3/5V	5	0.187 ± 0.020	5992 ± 13	4.23 ± 0.05	3.80 ± 0.02
TUCh 7600-0516	K1	5	0.249 ± 0.020	5163 ± 31	4.63 ± 0.06	3.56 ± 0.02
TYC 5882-1169	K3/4	5	0.241 ± 0.022	4939 ± 34	4.65 ± 0.09	3.05 ± 0.11
TYC 7065-0879N	K4	3	0.259 ± 0.020	5513 ± 28	4.58 ± 0.07	3.63 ± 0.03
TYC 7065-0879S	K4	3	0.267 ± 0.021	5453 ± 31	4.70 ± 0.14	3.63 ± 0.03

NOTE. — all uncertainties are internal, derived from the scatter of fitted values from individual spectra from the mean. The external uncertainties are much larger (see §4.5). All spectral types from Zuckerman & Song (2004)
[a] Lithium abundance could not be measured due to high rotational broadening in HIP 108422 ($v\sin i = 139.80$ km/s)

TABLE 6
RESULTS FOR STARS IN AB DORADUS (ABD)

Object ID	Sp.T.	# Obs.	EW_{6708} (Å)	T_{eff} (K)	$\log g$	$\log N_{Li}$
AB Dor	K1	3	0.261 ± 0.021	5210 ± 34	4.63 ± 0.06	3.50 ± 0.04
GSC 08894-00426	M2	3	0.037 ± 0.022	3343 ± 11	4.83 ± 0.05	0.25 ± 0.02
HD 13482A	K1	2	0.124 ± 0.020	5725 ± 105	4.47 ± 0.18	3.17 ± 0.03
HD 13482B		1	0.076 ± 0.020	5090 ± 10	4.95 ± 0.05	1.75 ± 0.02
HD 17332B		1	0.168 ± 0.020	5780 ± 10	4.35 ± 0.05	3.55 ± 0.02
HD 217343	G3V	3	0.172 ± 0.020	5957 ± 28	4.25 ± 0.05	3.68 ± 0.04
HD 217379N		2	0.020 ± 0.020	4050 ± 14	5.07 ± 0.06	0.30 ± 0.05
HD 217379S		2	0.030 ± 0.021	4165 ± 11	5.05 ± 0.07	0.35 ± 0.05
HD 218860	G5	2	0.222 ± 0.020	5670 ± 10	4.32 ± 0.06	3.55 ± 0.02
HD 224228	K3V	2	0.076 ± 0.020	4905 ± 11	4.82 ± 0.06	1.35 ± 0.02
HD 35650	K7	4	0.020 ± 0.020	4252 ± 10	5.06 ± 0.05	0.25 ± 0.02
HD 45270	G1V	3	0.142 ± 0.020	6187 ± 24	4.50 ± 0.10	3.90 ± 0.04
HD 65569	K1V	3	0.155 ± 0.020	5223 ± 31	4.87 ± 0.05	2.77 ± 0.03
HIP 14807	K6	1	0.034 ± 0.020	4500 ± 10	4.60 ± 0.05	0.55 ± 0.02
HIP 14809	G5	1	0.150 ± 0.020	6050 ± 10	4.25 ± 0.05	3.60 ± 0.02
HIP 17695	M3	2	0.074 ± 0.029	3545 ± 18	4.72 ± 0.06	0.25 ± 0.02
HIP 26369	K7	3	0.044 ± 0.020	4010 ± 15	4.55 ± 0.06	0.25 ± 0.02
HIP 31878	K7	3	0.042 ± 0.024	4240 ± 14	5.12 ± 0.05	0.53 ± 0.03
HIP 6276	G8	3	0.153 ± 0.020	5643 ± 13	4.43 ± 0.05	3.22 ± 0.04
HR 2468	G1.5	2	0.138 ± 0.020	6060 ± 14	4.60 ± 0.11	3.58 ± 0.03
UY Pic	K0V	3	0.267 ± 0.020	5600 ± 15	5.05 ± 0.06	3.60 ± 0.02
V372 Pub	M3	5	0.020 ± 0.021	3688 ± 19	4.88 ± 0.05	0.25 ± 0.02

NOTE. — all uncertainties are internal, derived from the scatter of fitted values from individual spectra from the mean. The external uncertainties are much larger (see §4.5). All spectral types from Zuckerman & Song (2004)

TABLE 7
RESULTS FOR THE FIELD STARS (RADIAL VELOCITY STANDARDS)

Object ID	Sp.T.	# Obs.	T_{eff} (K)	$\log g$	$\log N_{Li}$
GJ 729	M3.5	1	3340 ± 10	5.00 ± 0.05	0.25 ± 0.02
GJ 156	K7	4	4110 ± 11	5.19 ± 0.05	0.25 ± 0.02
Gl 205	M1.5	4	3875 ± 10	4.89 ± 0.06	0.25 ± 0.02
Gl 349	K3	5	4712 ± 24	4.79 ± 0.07	0.35 ± 0.02
Gl 382	M1.5	2	3745 ± 11	4.68 ± 0.06	0.25 ± 0.03
Gl 876	M4	1	3290 ± 10	4.60 ± 0.05	0.25 ± 0.02
Gl 880	M1.5	2	3795 ± 11	4.97 ± 0.06	0.25 ± 0.02
HD 103932	K5	5	4360 ± 10	4.77 ± 0.05	0.25 ± 0.02
HD 111631	K7	5	4073 ± 10	5.19 ± 0.05	0.25 ± 0.02
HD 153458	G0	2	5935 ± 11	4.12 ± 0.06	2.25 ± 0.02
HD 172051	G5V	3	6070 ± 12	4.45 ± 0.06	0.97 ± 0.03
HD 120467	K4	5	4231 ± 11	4.97 ± 0.05	0.25 ± 0.02
HD 83443	K0	3	5280 ± 12	3.90 ± 0.06	0.45 ± 0.02
HD 87359	G5	3	5903 ± 35	4.15 ± 0.05	0.92 ± 0.04
HD 88218	F8	1	6240 ± 10	4.10 ± 0.05	2.80 ± 0.02
HD 92945	K1	1	5310 ± 10	4.70 ± 0.05	2.95 ± 0.02
HD 96700	G2	1	6160 ± 10	4.20 ± 0.05	1.55 ± 0.02
LHS 1763	K5	4	4348 ± 10	4.78 ± 0.05	0.49 ± 0.02
NSV 2863	M1.5	4	3882 ± 11	4.94 ± 0.06	0.25 ± 0.02
NSV 6431	M2	5	3724 ± 10	4.64 ± 0.05	0.25 ± 0.02

NOTE. — all uncertainties are internal, derived from the scatter of fitted values from individual spectra from the mean. The external uncertainties are much larger (see §4.5).